Smart Structures and Systems, *Vol. 26, No. 4 (2020) 419-433*
DOI: https://doi.org/10.12989/sss.2020.26.4.419

Modal tracking of seismically-excited buildings using stochastic system identification

Chia-Ming Chang* and Jau-Yu Chou[a]

Department of Civil Engineering, National Taiwan University, No.1, Sec. 4, Roosevelt Road, Taipei 10617, Taiwan

(*Received September 28, 2019, Revised March 20, 2020, Accepted July 20, 2020*)

Abstract. Investigation of structural integrity has been a critical issue in the field of civil engineering for years. Visual inspection is one of the most available methods to explore deteriorative components in structures. Still, this method is not applicable to invisible damage of structures. Alternatively, system identification methods are capable of tracking modal properties of structures over time. The deviation of these dynamic properties can serve as indicators to access structural integrity. In this study, a modal tracking technique using frequency-domain system identification from seismic responses of structures is proposed. The method first segments the measured signals into overlapped sequential portions and then establishes multiple Hankel matrices. Each Hankel matrix is then converted to the frequency domain, and a temporal-average frequency-domain Hankel matrix can be calculated. This study also proposes the frequency band selection that can divide the frequency-domain Hankel matrix into several portions in accordance with referenced natural frequencies. Once these referenced natural frequencies are unavailable, the first few right singular vectors by the singular value decomposition can offer these references. Finally, the frequency-domain stochastic subspace identification tracks the natural frequencies and mode shapes of structures through quick stabilization diagrams. To evaluate performance of the proposed method, a numerical study is carried out. Moreover, the long-term monitoring strong motion records at a specific site are exploited to assess the tracking performance. As seen in results, the proposed method is capable of tracking modal properties through seismic responses of structures.

Keywords: operational modal analysis; frequency-domain stochastic subspace system identification; modal tracking; frequency band selection; strong motion records

1. Introduction

Structures may experience extreme loadings such as earthquakes or strong winds. These natural disasters can cause damage in structural components, which cannot be visibly observed by engineers due to nonstructural components (e.g., partition walls). Furthermore, structural collapse may occur if structural damage deteriorates to a certain level. Fortunately, modal tracking techniques can be applied to monitor the condition of a structure.

A modal tracking should yield a certain level of consistency and accuracy of identified modal properties. In literature, Verboven (2002) proposed a Mode Quality Index (MQI) to investigate the identified modal properties. Reynders *et al.* (2012) introduced several methods to ensure extracting high-quality modal properties from the measurements. Additionally, the excitation, temperature, and measurement noise will affect the modal properties and result in introducing uncertainties to the identification (Wu *et al.* 2017). The measurement noise during identification can be eliminated by the uncertainty bounds (Pintelon *et al.* 2007). Reynders and Maes (2017) proposed a method to quantify the uncertainties of identified mode shapes. These studies not only discussed the large variations during modal tracking but also the importance of the quality during modal tracking.

Modal properties such as natural frequencies, damping, and mode shapes can serve as an indicator to represent soundness of structures (Farrar and Doebling 1997, Mao *et al.* 2019). In practice, the Operational Modal Analysis (OMA) explores modal properties only based on structural responses. OMA can be distinguished into two main categories: time domain and frequency domain. In time domain OMAs, Stochastic Subspace system Identification (SSI) is one of well-known identification techniques (Loh *et al.* 2012, Wu *et al.* 2016). SSI establishes a mathematical model through structural response in the stochastic sense. Modal properties can be identified through this stochastic model. In past, Van Overschee and De Moor (1991) developed the stochastic subspace system identification method based on the matrix orthogonal projection that derives a stochastic state-space representation from the extended observability and controllability matrices. However, not only structural modes will be identified, but many spurious modes were also observed. In 2001, Peeters and De Roeck improved the identification quality by adding a stabilization diagram to SSI. This improvement will eliminate spurious modes and retain stable modes (i.e., structural modes). Moreover, Chang and Loh (2015) proposed an improved stochastic subspace system

*Corresponding author, Associate Professor,
E-mail: changcm@ntu.edu.tw
[a] Student, E-mail: d06521008@ntu.edu.tw

ISSN: 1738-1584 (Print), 1738-1991 (Online)

identification method by considering the singular spectrum analysis to reconstruct the measurements before applying to SSI. An efficient projection method was proposed to reduce the computational time. Still, the algorithms are time-consuming due to the enormous size of the Hankel matrix and a large number of system orders to be used. Moreover, time-domain SSI usually requires to resample the data to a low-frequency range to gain better resolution of identification results, and this signal preprocessing will affect the ability of identifying modes in high frequencies.

In the frequency domain, the Frequency Domain Decomposition (FDD) is one of the approaches that can carry out operational modal analysis based on the spectral representation of the measured signals in the eigen domain (Brincker *et al*. 2001). This method exploits the peak-picking method to obtain the natural frequencies of which the resolution depends on the spectral lines, i.e., the number of discrete Fourier transform points. The true modal frequencies may not show up in the spectrums. Thus, the number of discrete Fourier transform points should be sufficiently large to achieve the desired resolution. In addition, the stochastic subspace system identification can also be carried out in the frequency domain. McKelvey *et al*. (1996) proposed a subspace-based multivariable frequency-domain system identification method which employed the subspace system identification method in the frequency domain. Cauberghe (2004) extended this method into OMA by forming a Hankel matrix using frequency-domain responses, which were calculated by the discrete Fourier transform to the time-domain responses. Then, a stabilization diagram was employed to obtain the modal properties of a structure. As a result, the size reduction of the Hankel matrix (i.e., only half spectrum employed) alleviates the computational loading. Moreover, the efficiency can also be improved by a pre-defined frequency bands for a specific mode (Verboven 2002, Cauberghe 2004).

Some OMA methods have been proven to be appropriate for seismic responses (Pioldi and Rizzi 2017). Welch (1967) developed power spectrum using a time averaging approach to adjust the effects of irrational input signals. Pioldi *et al*. (2015) developed a refined Frequency Domain Decomposition (rFDD) to extend the input from ambient vibration to seismic excitation in FDD. The rFDD method was later applied to 22 seismic records to evaluate the effectiveness of the method (Pioldi and Rizzi 2017). Moreover, Pansieri (2016) developed and validated an improved data-driven stochastic subspace system identification to identify modal properties from seismic responses. With these improvements and extensions, modal properties can also be accurately and correctly extracted from seismic responses.

The objective of this study is to develop an improved modal tracking method based on seismic responses using frequency-domain stochastic subspace identification. In this method, a temporal-average frequency-domain Hankel matrix is first constructed using segmented portions of measurements, which also consider overlapped segments. This temporal averaging avoids a concentrated frequency content being used in the system identification, in particular of strong portions during earthquakes. Then, singular value decomposition is applied to the frequency-domain Hankel matrix, and a peak-picking method is utilized to the right-singular vectors to determine referenced natural frequencies. Multiple frequency bands can be obtained in accordance with the referenced natural frequencies. These frequency bands directly eliminate spurious modes to be obtained during continuous modal tracking and expedite the later process in stochastic subspace system identification. The frequency-domain Hankel matrix is subsequently divided into several portion with respect to these frequency bands. Modal properties can be finally identified band by band with a quick stabilization diagram. An eight-story lumped-mass model is numerically developed to evaluate performance of the proposed method for seismic responses. The results are compared with the real mode shapes and natural frequencies. Moreover, long-term strong motion records are adopted to observe the changes of modal properties over time using the proposed method. As a result, the proposed method is capable of identifying modal properties from seismic responses including high-frequency modes and holds a certain level of consistency to track modal properties.

2. Frequency-domain modal tracking method

In this study, a frequency-domain output-only system identification method is proposed. This method extends the conventional frequency-domain stochastic subspace identification method by using a temporal-averaged frequency-domain Hankel matrix (Welch 1967) to decrease the affection of energy distribution due to irrational inputs, such as seismic excitation. Moreover, Singular Value Decomposition (SVD) through a moving window on the frequency-domain Hankel matrix is utilized to find possible modes within a certain frequency band. This procedure narrows the Hankel matrix size in a frequency band which expedites the establishment of stabilization diagrams from the frequency-domain SSI. Each step of the proposed method is introduced in the following sections.

2.1 Frequency-domain stochastic subspace identification

Consider a discrete-time stochastic state-space model given by

$$\boldsymbol{x}[t+1] = \boldsymbol{A}\boldsymbol{x}[t] + \boldsymbol{w}[t], \ \ \boldsymbol{y}[t] = \boldsymbol{C}\boldsymbol{x}[t] + \boldsymbol{v}[t] \tag{1}$$

where $\boldsymbol{x}$ and $\boldsymbol{y}$ are the state and output measurement vector at time step t, respectively; $\boldsymbol{A}$ is the system matrix; $\boldsymbol{C}$ is the measurement matrix; $\boldsymbol{w}$ and $\boldsymbol{v}$ are the input and output Gaussian noise with a zero mean. For N samples of $\boldsymbol{y}$ in Eq. (1), the samples can be formed into a time-domain Hankel matrix such a

$$\boldsymbol{H} = \begin{bmatrix} \boldsymbol{y}[1] & \boldsymbol{y}[2] & \cdots & \boldsymbol{y}[p] \\ \boldsymbol{y}[2] & \boldsymbol{y}[3] & \cdots & \boldsymbol{y}[p+1] \\ \vdots & \vdots & \ddots & \vdots \\ \boldsymbol{y}[N-p+1] & \boldsymbol{y}[N-p+2] & \cdots & \boldsymbol{y}[N] \end{bmatrix} \tag{2}$$

where $\boldsymbol{H}$ is the Hankel matrix; p is the window length. A row criterion is applied to assure the observability of the first mode (Loh *et al*. 2012), which is given by

$$N - p + 1 > \frac{f_s}{2\omega_1} \tag{3}$$

where f_s is the sampling rate, and ω_1 is the first mode natural frequency. As mentioned in McKelvey and Viberg (2001), the time-domain stochastic state-space system in Eq. (1) can be converted into frequency domain using the Fourier transform. Therefore, each time-domain Hankel matrix in Eq. (2) can be then applied with the discrete Fourier transform to each row in $\boldsymbol{H}$, and the frequency-domain Hankel matrix can be constructed as

$$\boldsymbol{\mathcal{H}} = \begin{bmatrix} \boldsymbol{Y}[0] & \boldsymbol{Y}[1] & \cdots & \boldsymbol{Y}[p] \\ W_p^{-1}\boldsymbol{Y}[0] & W_p^{-1}\boldsymbol{Y}[1] & \cdots & W_p^{-1}\boldsymbol{Y}[p] \\ \vdots & \vdots & \ddots & \vdots \\ W_p^{-(N-p)}\boldsymbol{Y}[0] & W_p^{-(N-p)}\boldsymbol{Y}[1] & \cdots & W_p^{-(N-p)}\boldsymbol{Y}[p] \end{bmatrix} \tag{4}$$

where $\boldsymbol{\mathcal{H}}$ denotes the frequency-domain Hankel matrix; W_p^n represents the phase shift which will not affect the identification results (Chang and Huang 2017). Note that only the responses on $[0, \pi]$ are presented in the Hankel matrix $\boldsymbol{\mathcal{H}}$ in Eq. (4) due to the symmetry property, resulting in a reduced dimension as compared to the Hankel matrix $\boldsymbol{H}$ in Eq. (2). The Hankel matrix, $\boldsymbol{\mathcal{H}}$, can be divided into the past and future portions such as

$$\boldsymbol{\mathcal{H}} = \left[\frac{Y_p}{Y_f}\right] = \left[\begin{array}{cccc} \boldsymbol{Y}[0] & \boldsymbol{Y}[1] & \cdots & \boldsymbol{Y}[p] \\ W_p^{-1}\boldsymbol{Y}[0] & W_p^{-1}\boldsymbol{Y}[1] & \cdots & W_p^{-1}\boldsymbol{Y}[p] \\ \vdots & \vdots & \ddots & \vdots \\ W_p^{-(n-1)}\boldsymbol{Y}[0] & W_p^{-(n-1)}\boldsymbol{Y}[1] & \cdots & W_p^{-(n-1)}\boldsymbol{Y}[p] \\ \hline W_p^{-(n)}\boldsymbol{Y}[0] & W_p^{-(n)}\boldsymbol{Y}[1] & \cdots & W_p^{-(n)}\boldsymbol{Y}[p] \\ W_p^{-(n+1)}\boldsymbol{Y}[0] & W_p^{-(n+1)}\boldsymbol{Y}[1] & \cdots & W_p^{-(n+1)}\boldsymbol{Y}[p] \\ \vdots & \vdots & \ddots & \vdots \\ W_p^{-(n-p)}\boldsymbol{Y}[0] & W_p^{-(n-p)}\boldsymbol{Y}[1] & \cdots & W_p^{-(n-p)}\boldsymbol{Y}[p] \end{array}\right] \tag{5}$$

where $\boldsymbol{Y}_p$ represents the past portion matrix; $\boldsymbol{Y}_f$ represents the future portion matrix; $n = (N - p)/2$. The projection subspace can be determined by the past and future Hankel matrix defined as

$$\boldsymbol{O} = \boldsymbol{Y}_p/\boldsymbol{Y}_f = \boldsymbol{Y}_f\boldsymbol{Y}_p{}^T(\boldsymbol{Y}_p\boldsymbol{Y}_p{}^T)^{-1}\boldsymbol{Y}_p \tag{6}$$

where $\boldsymbol{O}$ is the projection of the past Hankel matrix on the future Hankel matrix by $\boldsymbol{Y}_p/\boldsymbol{Y}_f$ indicates. As mentioned in Chang and Loh (2015), an efficient projection method can be utilized to accelerate the calculation of the projection. The efficient projection is written by

$$\boldsymbol{Y}_p/\boldsymbol{Y}_f \cong \boldsymbol{Y}_f\boldsymbol{V}_{p,m}\boldsymbol{V}_{p,m}^T \rightarrow \boldsymbol{Y}_f\boldsymbol{V}_{p,m} \tag{7}$$

where $\boldsymbol{V}_{p,m}^T$ is neglected because the matrix can be a similarity matrix to both extended observability and controllability matrices in the SSI theory. Moreover, because the subspace, $\boldsymbol{O}$, represents a product of the extend observability and controllability matrices, SVD is used to separate the two matrices. The system matrix $\boldsymbol{A}_{id}$ and the measurement matrix $\boldsymbol{C}_{id}$ are calculated by

$$\begin{gathered} \boldsymbol{Y}_f\boldsymbol{V}_{p,m} = \boldsymbol{U}_{id,m}\boldsymbol{S}_{id,m}\boldsymbol{V}_{id,m}^T + \boldsymbol{U}_{id,0}\boldsymbol{S}_{id,0}\boldsymbol{V}_{id,0}^T \\ \boldsymbol{\Gamma} = \boldsymbol{U}_{id,m} = \begin{bmatrix} \boldsymbol{C}_{id} \\ \boldsymbol{C}_{id}\boldsymbol{A}_{id} \\ \boldsymbol{C}_{id}\boldsymbol{A}_{id}{}^2 \\ \vdots \\ \boldsymbol{C}_{id}\boldsymbol{A}_{id}{}^{n_s} \end{bmatrix}, \quad \boldsymbol{A}_{id} = \begin{bmatrix} \boldsymbol{C}_{id} \\ \boldsymbol{C}_{id}\boldsymbol{A}_{id} \\ \boldsymbol{C}_{id}\boldsymbol{A}_{id}{}^2 \\ \vdots \\ \boldsymbol{C}_{id}\boldsymbol{A}_{id}{}^{n_s-1} \end{bmatrix}^{\dagger} \begin{bmatrix} \boldsymbol{C}_{id}\boldsymbol{A}_{id} \\ \boldsymbol{C}_{id}\boldsymbol{A}_{id}{}^2 \\ \boldsymbol{C}_{id}\boldsymbol{A}_{id}{}^3 \\ \vdots \\ \boldsymbol{C}_{id}\boldsymbol{A}_{id}{}^{n_s} \end{bmatrix} \end{gathered} \tag{8}$$

where the subscripts "m" and "0" denote the main and redundant components in the product of the extended observability and controllability matrices; $\boldsymbol{\Gamma}$ represents the extended observability matrix; n_s is the number of state number; $(\,)^{\dagger}$ represents the pseudo inverse. The modal properties such as the natural frequencies, mode shapes, and damping ratios can be extracted from $\boldsymbol{A}_{id}$ and $\boldsymbol{C}_{id}$ by the eigen analysis. These modal parameters are obtained by

$$\begin{gathered} \boldsymbol{A}_{id}\boldsymbol{\eta} = \lambda_{id}\boldsymbol{\eta} \\ \frac{1}{\Delta t} ln(\lambda_{id}, \lambda_{id}{}^*) = -\xi\omega_n \pm j\omega_n\sqrt{1-\xi^2} \\ \boldsymbol{\varphi} = \boldsymbol{C}_{id}\boldsymbol{\eta} \end{gathered} \tag{9}$$

where λ_{id} is one of the eigenvalues in $\boldsymbol{A}_{id}$, $\lambda_{id}{}^*$ is the complex conjugate of λ_{id}; $\boldsymbol{\eta}$ is the eigenvector with respect to the state vector; ξ and ω_n are the damping ratio and natural frequency of a specific mode, respectively; $\boldsymbol{\varphi}$ is the mode shapes in complex domain. The real mode shapes can be obtained by rotating complex vectors to the real axis. Thus, the least square regression method is employed to determine the optimal rotation angles such that

$$\begin{gathered} \boldsymbol{Im}[\boldsymbol{\varphi}] = tan\theta\boldsymbol{Re}[\boldsymbol{\varphi}] \\ F_{obj} = arg\min_{\theta} ||\boldsymbol{Im}[\boldsymbol{\varphi}] - tan\theta\boldsymbol{Re}[\boldsymbol{\varphi}]||_2 \end{gathered} \tag{10}$$

where $\boldsymbol{Im}$ and $\boldsymbol{Re}$ indicate the imaginary and real parts of the mode shape, respectively; $\boldsymbol{F}_{obj}$ is the objective function which determines θ to minimize the distance between $\boldsymbol{Im}[\boldsymbol{\varphi}]$ and $tan\theta\boldsymbol{Re}[\boldsymbol{\varphi}]$; $||\cdot||_2$ is the L_2 norm. The mode shape $\boldsymbol{\varphi}$ can be finally converted to real numbers by rotating θ such as

$$\widehat{\boldsymbol{\varphi}} = e^{-j\theta}\boldsymbol{\varphi} \tag{11}$$

where $\widehat{\boldsymbol{\varphi}}$ is the mode shape in real number and $j = \sqrt{-1}$. By the aforementioned procedure, the modal properties can be identified.

2.2 Temporal-averaged frequency-domain Hankel matrix

To avoid certain energy concentrating in specific frequencies, the frequency-domain Hankel matrix should be modified. In the frequency domain, the frequency response can be averaged. Thus, the entire seismic responses are

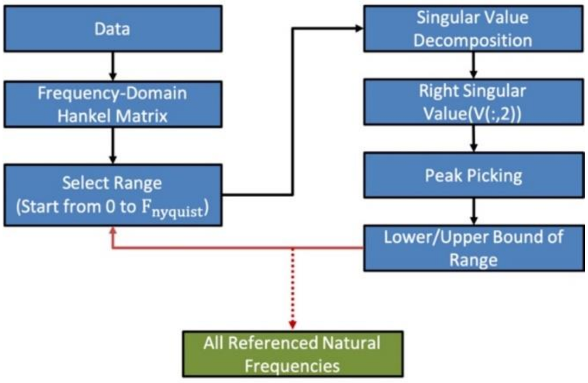

Fig. 1 Determination of referenced natural frequencies

sequentially segmented with some overlapped portions. By Eqs. (2)-(4), a series of frequency-domain Hankel matrices can be obtained. Consequently, the temporal-averaged Hankel matrix is calculated from the segmented Hankel matrices which is aligned with the Welch's theory (Welch 1967). This averaged Hankel matrix approximately contains even energy in each spectral line over frequencies. By reconsidering the measurement y in Eq. (1), the total samples N can be divided into k sequential portions with ℓ samples overlapped. The length of each portion will be $\frac{1}{k}(N-\ell)+\ell$. Each segmented portion can be formed into a time-domain Hankel matrix such as

$$\boldsymbol{H}_i=\begin{bmatrix} \boldsymbol{y}_i[1] & \boldsymbol{y}_i[2] & \cdots & \boldsymbol{y}_i[p] \\ \boldsymbol{y}_i[2] & \boldsymbol{y}_i[3] & \ddots & \boldsymbol{y}_i[p+1] \\ \vdots & \vdots & \ddots & \vdots \\ \boldsymbol{y}_i[m-p+1] & \boldsymbol{y}_i[m-p+2] & \cdots & \boldsymbol{y}_i[m] \end{bmatrix} \quad (12)$$

where $m=\frac{1}{k}(N-\ell)+\ell$; $\boldsymbol{H}_i$ is the Hankel matrix constructed from the i^{th} portion of samples, $1<i<k$; p is the window length. The Hankel matrices can be converted into the frequency domain through discrete Fourier transform such as in Eq. (4). The temporal-averaged frequency-domain Hankel matrix can be obtained from

$$\overline{\boldsymbol{\mathcal{H}}}=\frac{\boldsymbol{\mathcal{H}}_1+\boldsymbol{\mathcal{H}}_2+\cdots+\boldsymbol{\mathcal{H}}_k}{k} \quad (13)$$

where $\overline{\boldsymbol{\mathcal{H}}}$ is the temporal-averaged frequency-domain Hankel matrix; $\boldsymbol{\mathcal{H}}_i$ is a single frequency-domain Hankel matrix converted from Eq. (12). The temporal-averaged Hankel matrix, $\overline{\boldsymbol{\mathcal{H}}}$, is then applied to the SSI process from Eqs. (5)-(11).

2.3 Frequency band selection

Identifiable modes can be derived from the frequency-domain Hankel matrix in a certain frequency band near the natural frequencies. One advantage of the frequency-domain SSI is the selectable frequency band (Cauberghe 2004). In other words, the frequency-domain SSI can be employed in a frequency band of interest. In this study, a frequency band selection method for use in the frequency-domain SSI is developed. Consider the temporal-averaged Hankel matrix $\overline{\boldsymbol{\mathcal{H}}}$ in Eq. (13), and a window is applied to a certain frequency range of $\overline{\boldsymbol{\mathcal{H}}}$. In the beginning, this window has an identical frequency range up to the Nyquist frequency. The portion, $\overline{\boldsymbol{\mathcal{H}}}_L$, can be decomposed using Singular Value Decomposition (SVD) such as

$$\overline{\boldsymbol{\mathcal{H}}}_L\cong\boldsymbol{U}_L\boldsymbol{S}_L\boldsymbol{V}_L^T \quad (14)$$

where the subscript L denotes a portion of the Hankel matrix; $\boldsymbol{U}$ is the left singular vectors; $\boldsymbol{S}$ is the singular value matrix; $\boldsymbol{V}$ is the right singular vectors. To determine the dominant frequency components, only the first k singular values are considered in the SVD process, resulting in $\boldsymbol{U}\in\mathbb{R}^{(N-p+1)\times k}$, $\boldsymbol{S}\in\mathbb{R}^{k\times k}$, and $\boldsymbol{V}\in\mathbb{R}^{l\times k}$. A peak-picking method (Pavelka *et al.* 2017) is applied to the right singular vector V to determine a referenced natural frequency. This referenced natural frequency allows generating a corresponding frequency band. To find next referenced natural frequency, the previous referenced natural frequency divides the previously used frequency range into two portions. Repeating the same procedure, all referenced natural frequencies can be determined as illustrated in Fig. 1.

The width of a frequency band for a tentative mode can be determined by observing transfer function phase crossing the inflection point. For example, consider a system with a single mode (or a single pole) such that

$$H_{sys}(s)=\frac{1}{s^2+2\xi\omega_n s+\omega_n^2} \quad (15)$$

where H_{sys} is the system with a single mode; ω_n is the referenced natural frequency; ξ is the damping ratio; s is the Laplacian variable which is equal to $j\omega$, where $j=\sqrt{-1}$. The frequency band begins from the phase at almost 0° to -180°. By setting a threshold to the slope of the phase, the upper bound and lower bound of a referenced natural frequency and damping can be determined. Moreover, a scenario having two adjacent natural frequencies are considered such as

$$\begin{cases} \mathrm{F}_{L,c}\omega_c<\omega<\mathrm{F}_{U,c}\omega_c \cdots\cdots \text{when no overlapping} \\ \mathrm{F}_{L,c-1}\omega_{c-1}<\omega<\mathrm{F}_{U,c}\omega_c \cdots \text{when } \mathrm{F}_{L,c}\omega_c<\mathrm{F}_{U,c-1}\omega_{c-1} \\ \mathrm{F}_{L,c}\omega_c<\omega<\mathrm{F}_{U,c+1}\omega_{c+1} \cdots\cdots \text{when } \mathrm{F}_{U,c}\omega_c>\omega_{c+1} \end{cases} \quad (16)$$

where F_L and F_U represent the lower and upper bound factors, respectively; the subscript "c" denotes the currently picked mode. Thus, Fig. 2 illustrates the process which determines an effective frequency band with respect to picked natural frequencies. When the frequency band of a mode does not include other frequency bands or referenced natural frequencies, the effective frequency band is determined by multiplying the lower/upper bound factors that is shown in Fig. 2(a). Meanwhile, if the band contains other frequency bands, the frequency band must be modified. Fig. 2(b) shows that when the effective frequency bands of two modes are overlapped, the lower frequency bound is replaced by the upper bound of the previous band. Fig. 2(c) exhibits that when the effective frequency band contains another natural frequency, the derived frequency

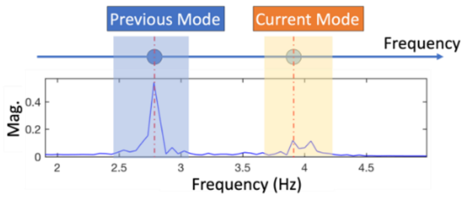

(a) Distinct modes

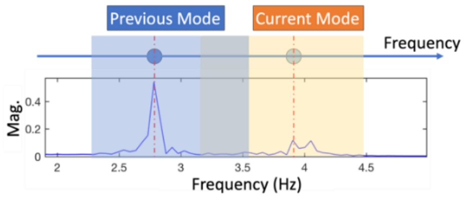

(b) Overlapping frequencies

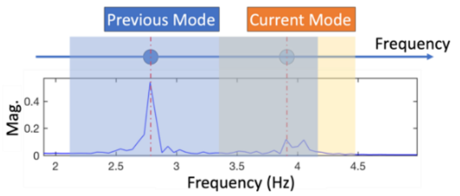

(c) Closely spaced modes

Fig. 2 Scenarios of effective frequency bands

bands of these two modes are merged into one frequency band.

2.4 Frequency-domain output-only system identification

Fig. 3 represents the flowchart of three scenarios considered in the modal tracking method. When the prior information is unknown (i.e., no referenced natural frequencies), users can employ the first scenario. Measured data are exploited to construct the temporal-averaged Hankel matrix (Eqs. (12)-(13)). The matrix is then utilized for frequency band selection (Eqs. (14)-(16)). After determining the frequency bands, the modal properties are identified by (Eqs. (7)-(11)) as the procedure shown in Fig. 3(a). A quick stabilization diagram is exploited with only 2 criteria to identify stable modes from the SSI process. First, the frequencies are checked using Eq. (17)

$$VAR = \frac{|\widehat{\omega}_n - \omega_n|}{\widehat{\omega}_n} \tag{17}$$

where $\widehat{\omega}_n$ is the referenced natural frequency determined from the band selection and ω_n is the identified frequency. The modes are considered as stable if VAR is lower than a threshold. Next, Modal Assurance Criterion (MAC) is applied to the identified modes and to determine consistent modes and is given by

$$MAC = \frac{\boldsymbol{\varphi}^T \widehat{\boldsymbol{\varphi}}}{|\boldsymbol{\varphi}||\widehat{\boldsymbol{\varphi}}|} \tag{18}$$

where $\boldsymbol{\varphi}$ and $\widehat{\boldsymbol{\varphi}}$ are identified mode shape in a quick stabilization diagram. When the MAC value is close to 1, meaning that the modes are consist and are stable. Meanwhile, when the value is close to 0, indicates that the modes are unstable and should be eliminated.

When the natural frequency references are available, the procedure becomes automated such as the 2nd and 3rd scenario in Figs. 3(b)-(c). The measurements are first used to construct the temporal-averaged Hankel matrix. The frequency bands are determined in accordance to the previously identified natural frequencies where ($\widehat{\omega}_n$ in Eq. (17) is replaced). Subsequently, the frequency-domain SSI is exploited to complete the modal tracking by the 2nd scenario.

Once the identified natural frequencies differentiate from the reference ones, the procedure can be switched to the 3rd scenario in Fig. 3(c). At this time, the frequency bands are re-identified by Eqs. (14)-(16). These re-identified frequency bands are used in the frequency-domain SSI, and the modal properties are consequently re-tracked.

3. Numerical example

An 8-story, shear-type building is established to numerically investigate performance of the proposed

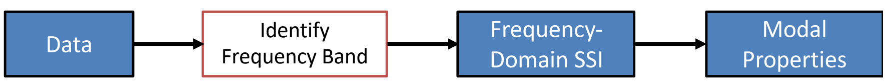

(a) 1st scenario for the first-time use

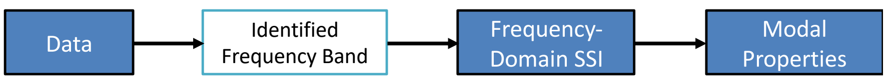

(b) 2nd scenario when identifying modal properties of interest

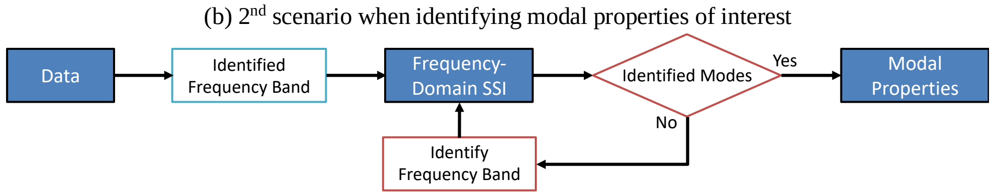

(c) 3rd scenario after the deviated natural frequencies are found

Fig. 3 Scenarios of the modal tracking method

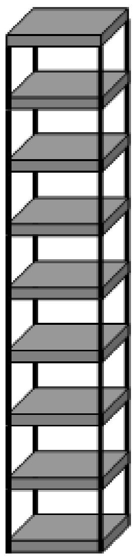

(a) Model illustration

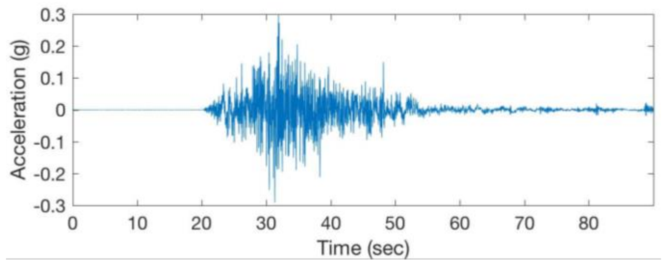

(b) Chi-Chi earthquake record at TCU071 with the PGA scaled to 0.3 g

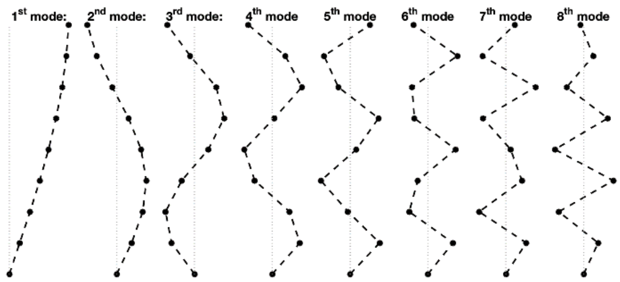

(c) Designed mode shapes

Fig. 4 Scenarios of the modal tracking method

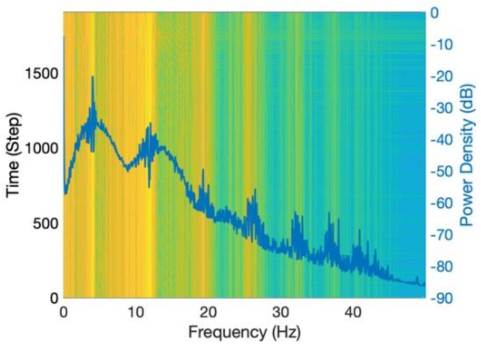

(a) Frequency content with temporal averaging

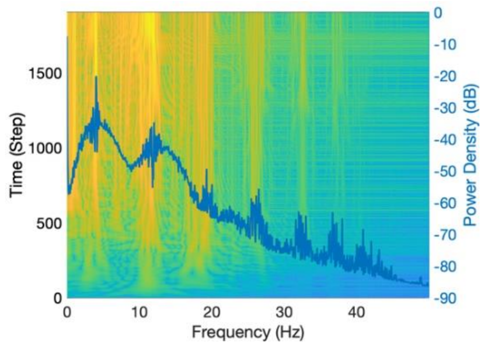

(b) Frequency content without temporal averaging

Fig. 5 Frequency content of 1st story

method under seismic excitation. In this model, the mass of this building is set to 100 kg each floor; the stiffness is 2 MN/m, 1.936 MN/m, 1.928 MN/m, 1.888 MN/m, 1.88 MN/m, 1.84 MN/m, 1.8 MN/m and 1.76 MN/m from the first floor to roof. The resulting natural frequencies are 4.07 Hz, 11.94 Hz, 19.41 Hz, 26.25 Hz, 32.14 Hz, 36.95 Hz, 40.54 Hz and 42.93 Hz. The modal damping is 0.02 for each mode. Fig. 4(a) illustrated the building model. In this study, the selected input ground motion is the 1999 Chi-Chi earthquake at the station of TCU071 of which the duration is 90 seconds with a sampling rate of 200 Hz. The peak ground acceleration of the excitation is scaled to a 0.3 g. The time history of the seismic excitation is shown in Fig. 4(b). Note that the ground acceleration is employed to generate structural response and does not participate in system identification. The designed mode shapes from the 1st mode to the 8th mode corresponding to the designed natural frequencies are illustrated in Fig. 4(c).

3.1 Frequency band selection

The frequency band selection is to determine the referenced natural frequencies as well as to generate a frequency-domain window for expediting the process of the frequency-domain stochastic system identification. First, the acceleration responses are divided into 4 portions with each having a 3/4 time-wise length overlapped. Each portion is used to establish time-domain Hankel matrices. The Hankel matrices are then converted to the frequency domain. The number of frequency points is 4,096. Note that the dimension can be reduced to half due to the symmetry property in the frequency domain. A temporal-averaged Hankel matrix is formed based on the multiple frequency-domain Hankel matrices along the frequency dimension using Eq. (13). Fig. 5 demonstrates the frequency content of the Hankel matrix regarding the first story with and without the temporal averaging. The color map provides the high to low intensities from light yellow to dark blue, while the blue curve is the mean power spectrum density all channel of sensors. As a result, the temporal averaging enhances the observability around the natural frequencies across the entire time steps (see Fig. 5(a)). Moreover, this temporal averaging can avoid a concentrated frequency content being used in system identification, i.e., around the first two

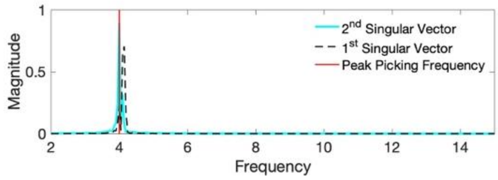

(a) Frequency content with temporal averaging

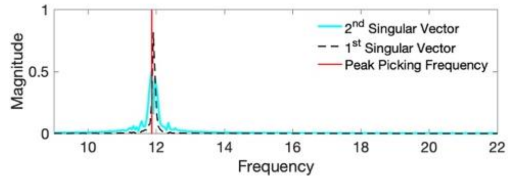

(b) Frequency content without temporal averaging

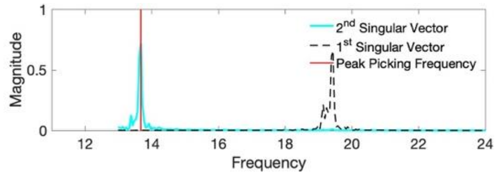

(c) Referenced natural frequency: 13.68 Hz

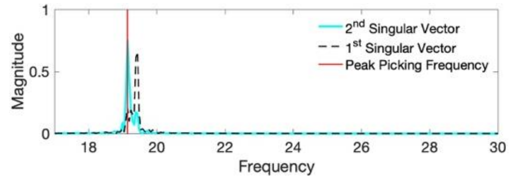

(d) Referenced natural frequency: 19.14 Hz

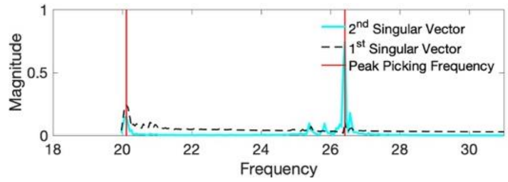

(e) Referenced natural frequencies: 20.11 Hz and 26.42 Hz

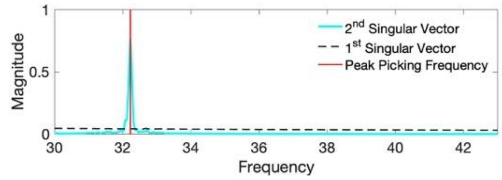

(f) Referenced natural frequency: 32.23 Hz

Fig. 6 Frequency band selection with a referenced natural frequency

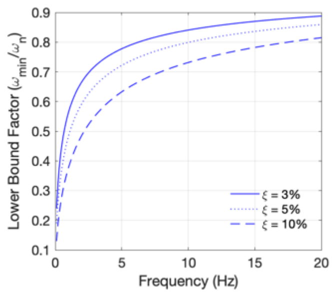

(a) Lower bound

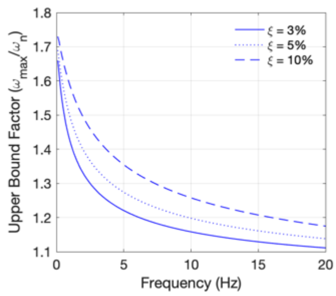

(b) Upper bound

Fig. 7 Multiplicative factor under different natural frequency and damping

modal frequencies in Fig. 5(a). Subsequently, only a few modes can be obtained in the identification results (see Fig. 5(b)). A window is utilized to select a certain frequency range from the Hankel matrix and then decomposed by singular value decomposition. Then, A peak-picking method (Pavelka and Huňady 2017) is applied to the right singular vector to determine the referenced natural frequencies.

Fig. 6 demonstrates the referenced natural frequencies determined by the proposed method. The black-dot curves indicate the 1st right singular vector, while the blue-solid curves indicate the 2nd right singular vector; the red-dash line are the referenced natural frequencies after considering peak picking to the 2nd right singular vectors (Pavelka *et al.* 2017). As shown in this figure, the peaks from the 1st right singular vector vanishes as determining frequency band in the high-frequency range (See Figs. 6(e)-(f))). Thus, additional right singular vector(s) (i.e., the 2nd right singular vector in this case) can help to relocate the referenced natural frequency.

To search the referenced natural frequencies, a window, which can extract the frequency range from 0 to 100 Hz (e.g., Nyquist frequency) of the temporal-averaged Hankel matrix, should be windowed with a maximized frequency range in the beginning (e.g., 0 Hz to the Nyquist frequency in this case). As shown in Fig. 6(a), the first determined referenced natural frequency is 4 Hz. Then, the selected frequency range of the Hankel matrix is updated to 5-100 Hz and 0-4 Hz for the second run. This process can avoid that 4Hz is not the lowest reference natural frequency. By repeating this process, and keep updating the lower bound and upper bound of the window, all referenced natural frequencies are determined. In this simulation, 13 referenced natural frequencies are 4.00 Hz, 11.87 Hz, 13.68 Hz, 14.51 Hz, 19.14 Hz, 20.11 Hz, 26.42 Hz, 32.23 Hz, 37.45 Hz, 40.28 Hz and 42.09 Hz. In this study, adjacent frequencies with difference lower than 3% are assumed to be the same referenced frequency. As shown in Fig. 6(e), this method can also extract two modes at once, meaning that the energy distribution in these two frequencies are similar. Note that some adjacent frequencies may result in same modal properties, and the frequency-domain SSI process can eliminate the spurious modes. Moreover, the SSI process can also check and identify closely spaced modes (Wu *et al.* 2017) in a single frequency band.

After determining referenced natural frequencies, each band width is calculated by Eq. (16). In the proposed

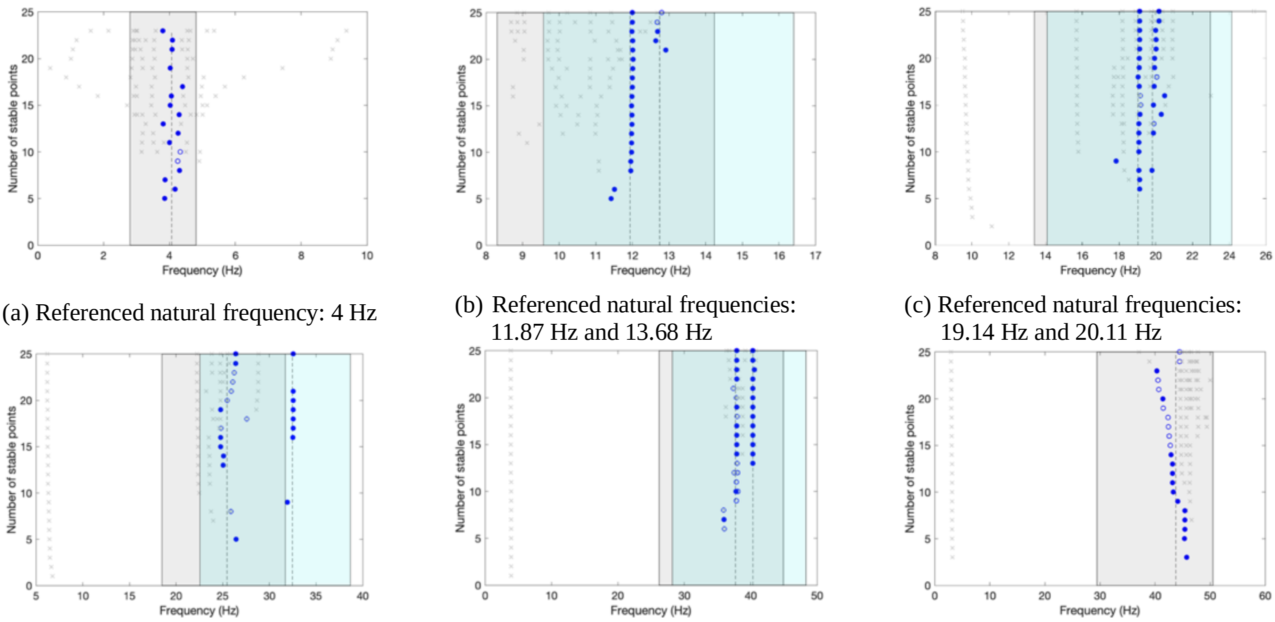

(a) Referenced natural frequency: 4 Hz

(b) Referenced natural frequencies: 11.87 Hz and 13.68 Hz

(c) Referenced natural frequencies: 19.14 Hz and 20.11 Hz

(d) Referenced natural frequencies: 26.42 Hz and 32.23 Hz

(e) Referenced natural frequencies: 37.45 Hz and 40.28 Hz

(f) Referenced natural frequency: 42.09 Hz

Fig. 8 Stabilization diagrams with respect to each frequency band of which the referenced natural frequencies

method, the lower and upper bounds of the frequency band is determined by searching the range where the slope of the phase at the referenced frequency is less than 0.1. Fig. 7 represents the lower and upper bounds factor regarding to a single degree of freedom system under different natural frequency and damping. Consequently, the lower bound factor converges at 0.8, while the upper bound factor converges at 1.2. The referenced natural frequencies are then applied to the categorizing rules (see Fig. 2). Then, the frequency bands are finally determined, and the Hankel matrix are separated by these bands and individually implemented in the frequency-domain SSI.

3.2 Stabilization diagram

The stabilization diagram used in this study employs much few modes to find stable modes. For example, the maximum system order in the stabilization diagram is 25. Fig. 8 represents the stabilization diagram of each revised frequency band. The identified modes are filtered using Eqs. (17)-(18). Moreover, Eq. (18) is used in adjacent identified modes to check if there are repeated modes. In the simulation, the results in different frequency bands with MAC larger than 0.6 are assumed to be the same mode, and are eliminated during the identification. As a result, the modes identified from the frequency-domain SSI are 4.07 Hz, 11.98 Hz, 19.05 Hz, 25.62 Hz, 32.21 Hz, 37.85 Hz, 40.22 Hz and 44.52 Hz.

In Fig. 8, the gray crosses indicate the poles corresponding to each system order; the blue-hollow circles indicate the ones satisfying the criterion in Eq. (17) (i.e., VAR $\leq$ 10%); the blue-solid circles indicate the poles concurrently satisfying two criteria in Eqs. (17)-(18) (i.e., MAC $\geq$ 0.9); the gray and light blue areas are the frequency bands in accordance with each referenced natural

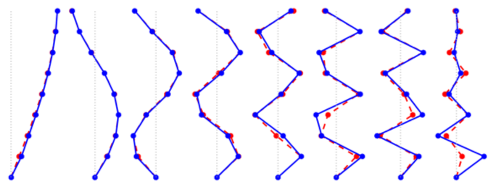

Fig. 9 Comparison between the designed mode shape and identified mode shape

frequency; these combined areas are the finally determined frequency band by the rules in Fig. 2. Moreover, Fig. 8(a) demonstrates the frequency-domain SSI while using a single mode identification. Fig. 8(b) exhibits when the frequency bands are overlapped, some referenced natural frequencies must be considered in one frequency band (See Fig. 2). In this case, two modes are identified at the same time in the process of the frequency-domain SSI. Moreover, to account for closely spaced modes, the modes are hardly observed since the natural frequencies are proximity. Alternatively, mode shapes can be served as an indicator to extract closely spaced modes (Wu *et al*. 2019). In this study, the closely spaced modes can be identified during comparing the MAC. When close modes exist, the first criterion (Eq. (17)) will extract all possible modes. Then, during the second criterion (Eq. (18)), multiple mode shapes will be extracted rather than only one.

To avoid identifying many modes at a time, which will cost much more time than extracting them one or few modes a time, the frequency bands are essential to narrow the extracting region and number of modes. Taking Fig. 8(c) as example, although the stabilization diagram shows a referenced natural frequency at about 10 Hz, the frequency bands restricts the identification from 13.5 Hz to 24.1 Hz. Additionally, frequency-bands with multiple referenced

Table 1 Comparison between the modal properties of the designed modes and the identified

Mode	1	2	3	4	5	6	7	8
NF_{true}	4.07 Hz	11.94 Hz	19.41 Hz	26.25 Hz	32.14 Hz	36.95 Hz	40.54 Hz	42.93 Hz
NF	4.07 Hz	11.98 Hz	19.05 Hz	25.62 Hz	32.21 Hz	37.85 Hz	40.22 Hz	44.52 Hz
VAR	0.1%	0.35%	1.8%	2.41%	0.22%	2.43%	0.78%	3.69%
MAC	1	1	1	0.99	0.97	0.94	0.96	0.54

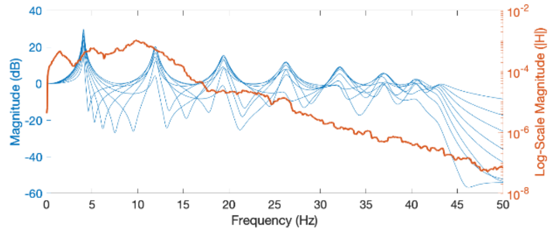

Fig. 10 Comparison between the transfer function of floor accelerations and the power spectral density of the earthquake record

natural frequencies should be identified together; otherwise, the modal properties of a certain mode can be incorrectly determined if these modes are identified one mode at a time.

3.3 Identification results

Fig. 9 illustrates the comparison between the designed and identified mode shapes. The blue lines indicate the identified mode shapes, while the red-dash lines indicate the designed mode shapes. As can be seen, the mode shapes have slightly differences in higher modes but are still comparable. In addition, the natural frequency error is calculated by VAR in Eq. (17), where $\widehat{\omega}_n$ is now replaced by the designed natural frequency. Moreover, the MAC in Eq. (18) is also applied to verifying the accuracy of the identified mode shapes, where $\widehat{\boldsymbol{\varphi}}$ represents the designed mode shapes. The results are listed in Table 1, where NF is the identified natural frequency; NF_{true} is the designed natural frequency. As found in this table, the first 7 modes are successfully identified with decent accuracy, and only the 8th mode has a good identified natural frequency without a high-quality mode shape.

Fig. 10 demonstrates the transfer functions of the 8-story model and the power spectral density (PSD) of the seismic ground motion. The blue curves represent the transfer functions of all floor accelerations, while the orange line represents the power spectrum of TCU071. As indicated in this figure, the energy distribution of the ground input tends to contribute more in low frequencies, and higher modes are barely excited (i.e., the 5th mode to the 8th mode). This finding highlights the performance of the proposed method, and higher modes can be still identified at a certain accuracy.

Moreover, the results obtained from the temporal-averaged Hankel matrix are compared to those from a single Hankel matrix by Eqs. (2)-(4). Table 2 represents the results based on one Hankel matrix without averaging. As seen in Tables 1 and 2, the higher modes can be identified when considering the temporal-averaged Hankel matrix. Additionally, the errors between the designed and identified natural frequencies are lower when employing the temporal-average Hankel matrix.

To investigate modal tracking performance of the proposed method, 100 sets of earthquake records from station ILA050 in Yilan, Taiwan is utilized to generate structural responses. In the investigation, both proposed method and conventional SSI (Cabboi *et al*. 2017) are employed for comparison. For the proposed method, the frequency bands are assumed to be known and employs the results in Fig. 8. Then, the modal tracking only requires the frequency-domain SSI process. Due to the length of the records, the number of frequency points (i.e., p in Eq. (5)) is changed from 4096 to 2048. The other parameters remain the same as the previous example. Meanwhile, the system order of the conventional SSI is 50, and the width of the Hankel matrix is 600. The success rate of each mode using the proposed method and using conventional SSI within 100 events are also listed in Table 3. The success rate is calculated using Eq. (19), where the # Total Events is 100; # MAC is the events that exceed threshold γ, which is set to 0.5. Moreover, the average MAC and VAR are calculated to compare the effectiveness of the proposed method with the conventional SSI for modal tracking from seismic responses.

$$\text{Success Rate} = \frac{\#\,\text{MAC} > \gamma}{\#\,\text{Total Events}} \tag{19}$$

Table 2 Comparison between the modal properties of the designed modes and the identified modes from the conventional Hankel matrix

Mode	1	2	3	4	5	6	7	8
NF_{true}	4.07 Hz	11.94 Hz	19.41 Hz	26.25 Hz	32.14 Hz	36.95 Hz	40.54 Hz	42.93 Hz
NF	4.21 Hz	11.43 Hz	19.30 Hz	25.82 Hz	N.A.	N.A.	N.A.	N.A.
VAR	3.26%	4.24%	0.55%	1.63%	N.A.	N.A.	N.A.	N.A.
MAC	1	0.99	1	0.98	N.A.	N.A.	N.A.	N.A.

Table 3 Investigation of modal tracking using 100 sets of seismic records

Mode	1	2	3	4	5	6	7	8
Proposed method								
Success Rate	96%	96%	83%	74%	82%	78%	87%	46%
VAR	1.4%	1.2%	1.9%	2.0%	1.4%	1.6%	2.5%	1.3%
MAC	1	1	0.99	0.97	0.94	0.92	0.71	0.69
Conventional SSI (Cabboi *et al*. 2017)								
Success Rate	74%	69%	84%	19%	0%	0%	0%	0%
VAR	1.4%	2.4%	1.5%	1.0%	N.A.	N.A.	N.A.	N.A.
MAC	1	0.99	0.99	0.99	N.A.	N.A.	N.A.	N.A.

Table 4 Comparison of the computational cost between the proposed method and the conventional SSI

Proposed method		Time-domain SSI (Cabboi *et al*. 2017)	
Method procedure	Consuming time	Method procedure	Consuming time
Forming Hankel matrix	8.2 sec	Forming Hankel matrix	31.9 sec
Frequency band selection	45.7 sec	Frequency band selection	0.2 sec
Frequency-domain SSI	5.1 sec	Frequency-domain SSI	0.27 sec
Total	59 sec	Total	32.37 sec

As indicated in Table 3, the proposed method is capable of identifying up to the 7th mode with a success rate higher than 70%. For the 8th mode, this method is still able to identify the modal properties in almost half of the events. Although the average MACs in the 7th and 8th modes of the proposed method are relatively low, the identified natural frequencies are still within decent accuracy. As for the conventional SSI, only the lower modes are successfully identified. The 4th mode shows a slightly high MAC and low VAR using the conventional SSI; however, the success rate is much lower than the proposed method. Therefore, the proposed method shows the capability of identifying lower modes with relative high accuracy as compared to the conventional SSI. Moreover, the proposed method also exhibits better performance of identifying modes in high frequencies.

Computational load is also evaluated in this study. Table 4 shows the time cost of both proposed method and the conventional SSI during each step of process when identifying the modal properties subjected to the TCU071 earthquake. As a result, the frequency-domain SSI is 6 times faster than the conventional SSI. In other words, after determining the frequency bands, the frequency-domain SSI can quickly identify structural modes in each frequency band.

Meanwhile, a number of spurious modes are first eliminated by the frequency bands. Moreover, the frequency band selection can be modified for faster determination with prior knowledge of the structure, such as changing the upper bound in the process. For instance, the time cost will decrease to 19 seconds if the upper bound is modified from 100 Hz to 50 Hz.

The proposed method generates the stabilization diagram with a certain range of frequencies in the Hankel matrix. Thus, the maximum number of system orders used can be lower. Fig. 11 demonstrates the stabilization diagram generated from the conventional SSI. Note that the system order used in the conventional SSI should be twice because the time-domain SSI results in a conjugate-pair eigenvalue. By comparing Fig. 11 with Fig. 8, the stabilization diagram from the conventional SSI is much more complex than the frequency-domain SSI, and more computational time is definitely expected in the conventional SSI.

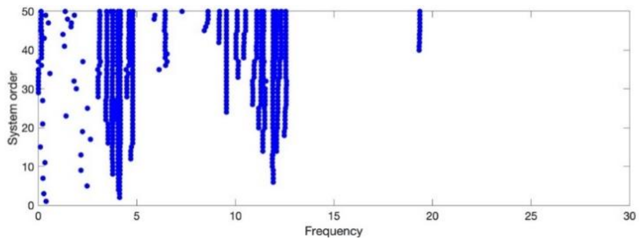

Fig. 11 Stabilization diagram of the time-domain SSI

4. Strong motion records

The long-term strong ground motion records of Civil and Environmental Engineering Department (CEED) Building at National Chung-Hsing University (NCHU) in Taiwan are employed to evaluate the effectiveness and consistency of the proposed method on modal tracking. Fig. 12(a) demonstrates the photo of the building. This building is a RC structure with 7-stories aboveground and 1-story underground. The length is 65.5 m, and the width is 37.5 m. The building is about 26.2 m tall. The 29 uniaxial accelerometers are distributed in the basement, 1F, 4F, and 7F. In this example, the responses measured along the lateral axes in the 4th and 7th floors are applied to the

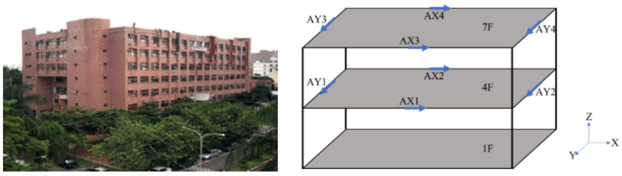

(a) (b)

Fig. 12 Civil and Environmental Engineering Department (CEED) building and sensor locations. (a) Photo of the field-testing building, (b) Accelerometer locations

proposed method. The sensing system can be considered as an output-only system because the input ground motion without structure-ground interaction is unavailable. As shown in Fig. 12(b), this example employs two x-direction and y-direction accelerations in the 4th and 7th floors. The data acquisition system began monitoring after the construction was completed in 1994. The building suffered the Chi-Chi earthquake in 1999 and resulted in moderate damage. After the Chi-Chi earthquake, this building was retrofitted in 2000.

In the field test, 178 data sets in 1994-2015 are applied to the proposed method. The data can be distinguished into three main stages: the healthy condition after construction in 1994-1999, moderate damage condition after the Chi-Chi earthquake in 1999-2000, and after-retrofit condition in 2000-2015. In the first stage, the structure is undamaged, and the responses are applied to the proposed method to extract modal properties. The number of frequency points selected is 4096, and the maximum system order used in the stabilization diagram is 50. Both x and y directions of floor accelerations are separately applied to the proposed method for single-axis modal properties. Then, both directions are combined together to analyze coupled mode shapes. The identified natural frequencies are 3.06 Hz, 3.12 Hz, 4.13 Hz, 8.72 Hz, 10.18 Hz and 10.38 Hz. Because the true modal properties of the structure are unavailable, the results are compared with those identified from the conventional SSI (Cabboi *et al.* 2017) and are listed in Table 5. The system order chosen in the conventional SSI is 120, and the length of Hankel matrix is 500. In the comparison, all six modes are determined with minor differences in the natural frequencies during the healthy stage. The mode shapes are compared in Fig. 13, where the blue-solid line represents the identified mode shapes from the proposed method, and the red-dash line represents the mode shapes based on the identified mode shapes from the proposed method, and the red-dash line represents the mode shapes based on the conventional SSI. From the figure, the mode shapes meet a good agreement, indicating the accuracy of the proposed method.

During Chi-Chi earthquake, six modes are still identified through seismic responses from the Chi-Chi earthquake event using the proposed method. Meanwhile, conventional SSI failed to identify the last mode. By observing Table 5, a 30-40% reduction is found in the natural frequencies in the first two modes, implying the occurrence of structural damage. These phenomena in the natural frequency reduction are also found in Hong *et al.* (2009). However, errors about 10% can be found in higher mode frequencies because the uncertainty during the earthquake can result in larger variations in identification. After structural retrofit, the identified natural frequency raises to 2.59 Hz, 2.63 Hz, 3.66 Hz, 7.51 Hz, 7.64 Hz and 9.96 Hz. The increment in the frequency can be seen as a success of the structural retrofit because the structural stiffness increases. As a result, the proposed method consistently yields the modal properties of the first six modes as compared to the conventional SSI.

Figs. 14 and 15 demonstrate the modal quality of the modal tracking around Chi-Chi earthquake and around structural retrofit. The modal quality is been exploited using

Table 5 Comparison of the natural frequencies between the proposed method and the conventional SSI during three stages

Stage	Methods	Mode 1	Mode 2	Mode 3	Mode 4	Mode 5	Mode 6
Healthy stage	Proposed method	3.06 Hz	3.12 Hz	4.13 Hz	8.72 Hz	10.18 Hz	10.38 Hz
	Conventional SSI	2.83 Hz	3.02 Hz	4.00 Hz	8.26 Hz	9.97 Hz	10.33 Hz
Damage stage	Proposed method	2.07 Hz	1.80 Hz	3.05 Hz	5.16 Hz	6.60 Hz	9.65 Hz
	Conventional SSI	2.01 Hz	1.97 Hz	2.71 Hz	4.75 Hz	7.21 Hz	N.A.
Retrofit stage	Proposed method	2.59 Hz	2.63 Hz	3.66 Hz	7.51 Hz	7.64 Hz	9.96 Hz
	Conventional SSI	2.64 Hz	2.67 Hz	3.53 Hz	7.58 Hz	8.32 Hz	10.21 Hz

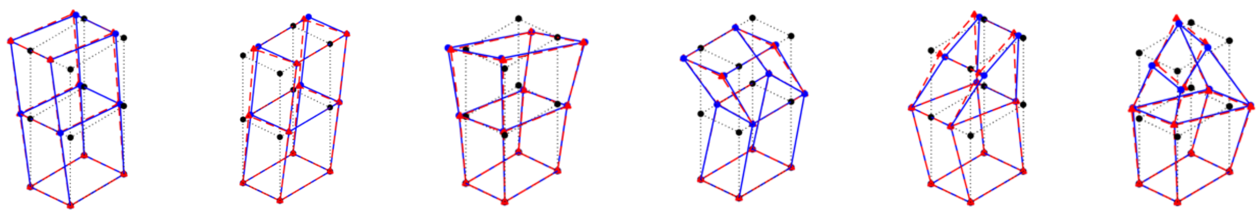

Mode 1 Mode 2 Mode 3 Mode 4 Mode 5 Mode 6

Fig. 13 Identified modes in the healthy stage (red-dash: conventional SSI, blue-solid: proposed method)

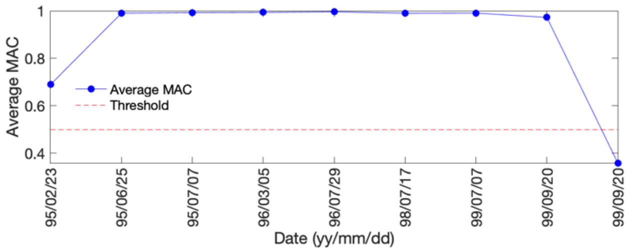

(a) MAC before/after Chi-Chi earthquake (99/09/20)

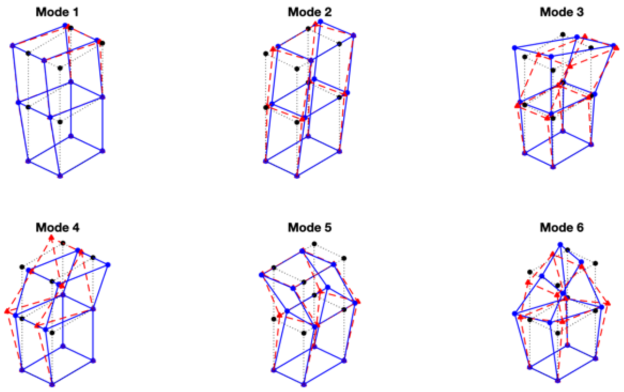

(b) Identified mode shapes based on different frequency bands (blue-solid: new, red-dash: old)

Fig. 14 Modal tracking results before/after Chi-Chi earthquakes

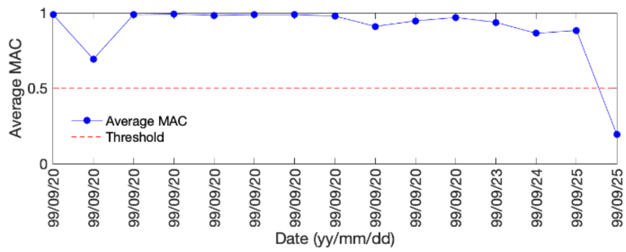

(a) MAC before/after structural retrofit

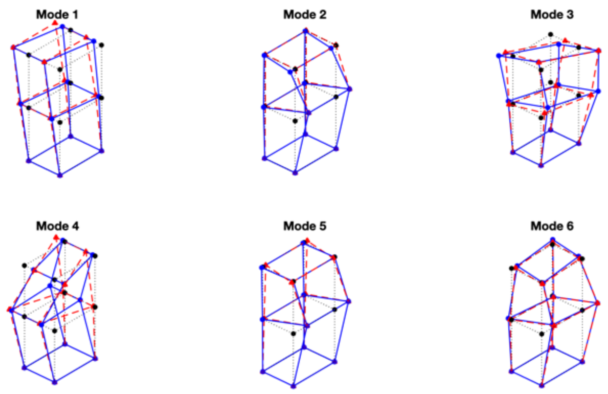

(b) Identified mode shapes using different frequency bands (blue-solid: new, red-dash: old)

Fig. 15 Modal tracking results before/after structural retrofit

MAC (Eq. (18)), where $\boldsymbol{\varphi}$ and $\hat{\boldsymbol{\varphi}}$ are the mode shapes of the current event and the previous event, respectively. As shown in Fig. 13(a), tracking using the frequency bands developed during the healthy stage has a sudden decrease during Chi-Chi earthquake by means of MACs, which indicate that the structure is damaged. Moreover, the suddenly decreased MAC to lower than 0.5 triggers the mechanism of re-determining the frequency bands. Fig. 14(b) represents the mode shapes using different frequency bands, where the red-dash line indicates mode shapes based on predefined frequency bands, and the blue-solid line indicates mode shapes based on re-determined frequency bands. These resulting modal properties are then considered as the new frequency bands for future modal tracking.

Fig. 15(a) demonstrates the MAC around structural retrofit. As shown in the figure, the MAC slowly decreases after the earthquake, indicating that the structure is under retrofit. On 1999/09/25, the MAC drops to 0.19, and the frequency bands need to be re-determined. Fig. 15(b) represents the comparison between the mode shapes using the frequency band determined from the previous event and the ones using the newly determined frequency bands. In the figure, the blue-solid line indicates the mode shapes using the newly determined frequency bands, while the red-dash line indicates mode shapes using the old frequency bands. The results indicate that the proposed method is capable of tracking modal properties after structural retrofit.

Fig. 16 represents the modal tracking of the 178 data sets comparing to conventional SSI method. In this figure, the gray-cross indicates the results from conventional SSI; while the blue-dot indicates the results from the proposed method. Figs. 16(b)-(c) are generated using the earthquake responses during the healthy stage and during the Chi-Chi earthquake. As seen in the figure, the natural frequencies drop during the earthquake, indicating that the structure is defected. After structural retrofit, the natural frequencies are increased. Therefore, the results not only exhibit the modal tracking effectiveness of the proposed method but also prove the success of the structural retrofit.

In addition, the modal quality during different stages using the two methods are demonstrated in Fig. 17. As shown in this figure, the gray-cross line indicates the conventional SSI, and the colored-circle indicates the proposed method. The success rate of each mode is calculated using Eq. (19); while the uncertainty by means of standard deviations based on MACs are calculated using Eq. (20)

$$\mathrm{STD} = \sqrt{\frac{1}{\#\,\text{Total Events} - 1} \sum_{i=1}^{\#\,\text{Total Events}} (\mathrm{MAC}_i - \overline{\mathrm{MAC}})^2} \quad (20)$$

where STD is the standard deviation; $\overline{\mathrm{MAC}}$ is the average MAC value within all events. In Fig. 17(a), the low standard deviation in first two modes indicate the accuracy of the proposed method. However, the success rate of the first mode is only 62%. This may be due to the excitation direction and ununiform energy distribution during the healthy stage. As for the last mode, the proposed method can identify about one third of the events. As a result, the proposed method is effective in tracking structural modes in low frequencies with high accuracy, and is capable of identifying comparable modes in high frequencies. On the other hand, although the conventional SSI can identify

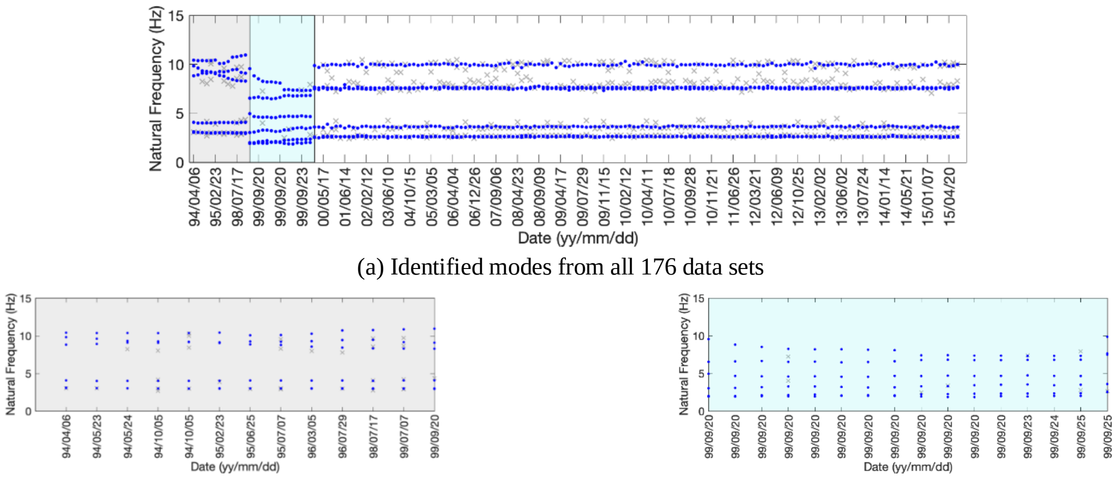

(a) Identified modes from all 176 data sets

(b) Identified modes at beginning stage

(c) Identified modes during damaged stage

Fig. 16 Modal tracking results

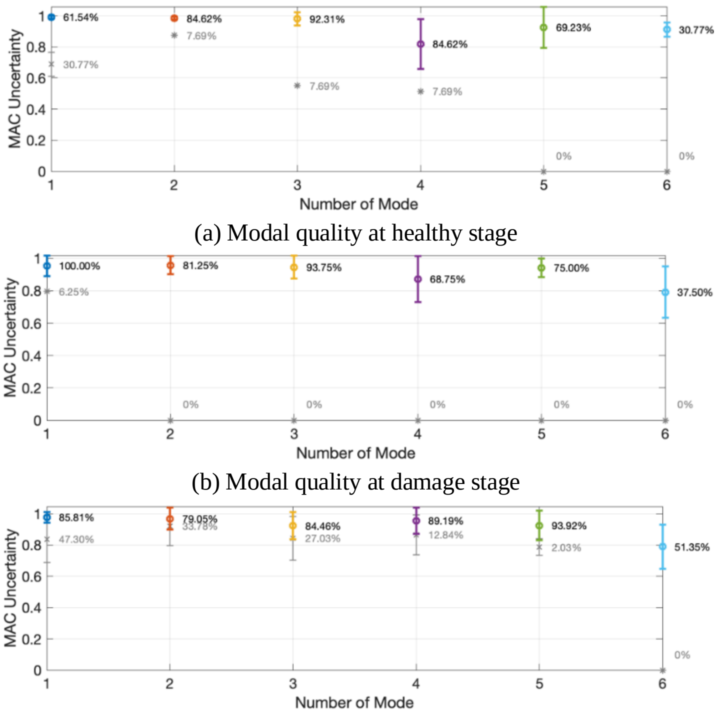

(a) Modal quality at healthy stage

(b) Modal quality at damage stage

(c) Modal quality at retrofit stage

Fig. 17 Modal quality

similar modes in shown in Fig. 17(b), the success rate is low. The modal quality from the conventional SSI is not as stable as the proposed method. Meanwhile, the result can be improved by considering different criteria during extraction of the stabilization diagram. Fig. 17(b) shows the modal quality during Chi-Chi earthquake. The proposed method is capable of identifying the first five modes with a high success rate so that the proposed method consistently yields modal properties during strong earthquake excitations. Meanwhile, conventional SSI could only track the first mode. Fig. 17(c) represents the modal quality after the structural retrofit. As shown in the figure, the standard deviation of the first five modes of both methods are low. Moreover, all of the success rates exceed 70% that again demonstrate the consistency in modal tracking using the proposed method and the effectiveness comparing to conventional SSI. Although the success rate of the last mode is only 50%, the proposed method can still provide decent performance because of the high MAC values.

5. Conclusions

In this study, a modal tracking technique based on seismic responses was proposed. The method first divided the structural responses into sequential portions and constructed multiple frequency-domain Hankel matrices. The frequency-domain Hankel matrices were used to compute a temporal-average frequency-domain Hankel matrix. The temporal averaging allowed averaging the energy content in the frequency-domain Hankel matrix and avoided the concentrated energy from the strong portions of seismic responses. Then, the proposed frequency band selection method was exploited to segment the average frequency-domain Hankel matrix into several portions. Each portion in the average frequency-domain Hankel matrix corresponded with a specific frequency band associated with one or more referenced natural frequencies. These referenced natural frequencies can be available from the peak-picking process of right singular vectors in Eq. (14) or previously identified natural frequency. Finally, modal properties can be extracted band by band using frequency-domain stochastic system identification.

In the numerical example, the proposed method was evaluated by a seismically-excited building to investigate identification accuracy and consistency. The proposed method was also compared to the conventional SSI method. After the frequency band is selected, the process of the proposed method can be automated and expedited and would be more efficient than the conventional SSI method. Moreover, the proposed method employed the Hankel matrix with a reduced dimension of the Hankel matrix. In addition, as seen in the results, the proposed method was able to extract all structural modes in terms of natural frequencies including those high-frequency modes. Up to the 7th mode out of 8 modes, at least 74% success rate implied the identification consistency of the proposed method. Only the 8th mode had a slightly low-quality mode shape due to low energy in high frequencies of seismic excitations. On the other hand, only first four modes can be identified by the time-domain SSI method. Therefore, the proposed frequency-domain system identification was numerically verified to be more capable of identifying seismically-excited buildings, in particular of higher modes.

To verify the effectiveness of the proposed method, the CEED building was investigated using strong motion records in 1994-2015. As found in the results, the modal properties (i.e., natural frequencies and mode shapes) were consistently tracked with at least five modes from seismic responses of the building. During the stages of structural damage or structural retrofit, the proposed method was able to re-identify the structural modes by the switching mechanism, such as the 3^{rd} scenario in Fig. 3. The modal quality of the first five modes remained a certain level of consistency. Because of low energy in high frequency content of earthquakes, the sixth mode had relatively large variations in terms of MAC. Therefore, the proposed method can consistently track modal properties once the frequency content of earthquakes had sufficient energy. The modal quality of successfully identified modes also validated the effectiveness of the proposed method.

Acknowledgments

This research is supported by the Ministry of Science and Technology in Taiwan under Grant Nos. MOST 104-2218-E-002-036 and MOST 107-3011-F-009-003.

References

Brincker, R., Zhang, L. and Andersen, P. (2001), "Modal identification of output-only systems using frequency domain decomposition", *Smart Mater. Struct.*, **10**(3), 441-445. https://doi.org/10.1088/0964-1726/10/3/303.

Cauberghe, B. (2004), "Applied frequency-domain system identification in the field of experimental and operational modal analysis", *Praca Doktorska*, VUB, Brussel, Belgium.

Chang, C.M. and Loh, C.H. (2015), "Improved stochastic subspace identification for structural health monitoring", *J. Phys. Conf. Ser. DAMAS 2015*, **628**(1), 012010. https://doi.org/10.1088/1742-6596/628/1/012010.

Chang, C.M. and Huang, S.K. (2017), "Stochastic subspace system identification using multivariate time-frequency distributions", *Proceedings of SPIE 10168, Sensors and Smart Structures Technologies for Civil, Mechanical and Aerospace Systems 2017*, Portland, Oregon, USA, April. https://doi.org/10.1117/12.2259993.

Cabboi, A., Magalhaes, F., Gentile, C. and Cunha, A. (2017), "Automated modal identification and tracking: Application to an iron arch bridge", *Struct. Control Health Monit.*, **24**(1), e1854. https://doi.org/10.1002/stc.1854.

Farrar, C.R. and Doebling, S.W. (1997), "An overview modal-based damage identification methods", *Proceedings of International Workshop DAMAS 97 Structural Damage Assessment Using Advanced Signal Processing Procedures*, Sheffield, UK, July.

Hong, A.L., Betti, R. and Lin, C.C. (2009), "Identification of dynamic models of a building structure using multiple earthquake records", *Struct. Control Health Monit.*, **16**(2), 178-199, 2009. https://doi.org/10.1002/stc.289.

Loh, C.H., Liu, Y.C. and Ni, Y.Q. (2012), "SSA-based stochastic subspace identification of structures from output-only vibration measurements", *Smart Struct. Syst., Int. J.*, **10**(4_5), 331-351. https://doi.org/10.12989/sss.2012.10.4_5.331.

Loh, C.H., Li, J.H. and Chao, S.H. (2012), "Application of singular spectrum analysis to identify the degrading structure using deteriorating distributed element model", *Earthq. Eng. Struct. Dyn.*, **42**(5), 743-761. https://doi.org/10.1002/eqe.2242.

McKelvey, T., Akcay, H. and Ljung, L. (1996), "Subspace-based multivariable system identification from frequency response data", *IEEE Trans. Automat. Contr.*, **41**(7), 960-979. https://doi.org/10.1109/9.508900.

McKelvey, T. and Viberg, M. (2001), "A robust frequency domain subspace algorithm for multi-component harmonic retrieval", *Proceedings of 35th Asilomar Conference on Signals, Systems and Computers*, Pacific Grove, CA, USA, November. https://doi.org/10.1109/ACSSC.2001.987698.

Mao, J.X., Wang, H. and Spencer Jr., B.F. (2019), "Gaussian mixture model for automated tracking of modal parameters of long-span bridge", *Smart Struct. Syst., Int. J.*, **24**(2), 243-256. https://doi.org/10.12989/sss.2019.24.2.243.

Peeters, B. and De Roeck, G. (2001), "Stochastic system identification for operational modal analysis: a review", *J. Dyn. Syst. Meas. Control*, **123**(4), 659-667. https://doi.org/10.1115/1.1410370.

Pintelon, R., Guillaume, P. and Schoukens, J. (2007), "Uncertainty calculation in (operational) modal analysis", *Mech. Syst. Signal Process.*, **21**(6), 2359-2373. https://doi.org/10.1016/j.ymssp.2006.11.007.

Pioldi, F., Ferrari, R. and Rizzi, E. (2015), "Output-only modal dynamic identification of frames by a refined FDD algorithm at seismic input and high damping", *Mech. Syst. Signal Process*, **68-69**, 265-291. https://doi.org/10.1016/j.ymssp.2015.07.004.

Pansieri, S. (2016), "Time domain output-only modal dynamic stochastic subspace identification algorithm for seismic applications", M.Sc. Dissertation, Universita` degli Studi di Bergamo, Bergamo, Italy.

Pioldi, F. and Rizzi, E. (2017), "Assessment of frequency versus time domain enhanced technique for response-only modal dynamic identification under seismic excitation", *Bull. Earthq. Eng*., **16**(3), 1547-1570. https://doi.org/10.1007/s10518-017-0259-7.

Pioldi, F. and Rizzi, E. (2017), "A refined frequency domain decomposition tool for structural modal monitoring in earthquake engineering", *Earthq. Eng. Eng. Vib*., **16**(3), 627-648. https://doi.org/10.1007/s11803-017-0394-9.

Pavelka, P., Huňady, R. and Kučinský, M. (2017), "Modal analysis using the signal processing toolbox of Matlab 2017", *Am. J. Mech. Eng*., **5**(6), 312-315. https://doi.org/10.12691/ajme-5-6-16.

Reynders, E., Houbrechts, J. and De Roeck, G. (2012), "Fully automated (operational) modal analysis", *Mech. Syst. Signal Process.*, **29**, 228-250. https://doi.org/10.1016/j.ymssp.2012.01.007.

Reynders, E. and Maes, K. (2017), "Uncertainty quantification of modal characteristics identified from frequency-domain stochastic subspace identification", *Procedia Eng*., **199**, 996-1001. https://doi.org/10.1016/j.proeng.2017.09.231.

Van Overschee, P. and De Moor, B. (1991), "Subspace algorithms for the stochastic identification problem", *Proceedings of the 30th IEEE Conference on Decision and Control*, Brighton, UK, December. https://doi.org/10.1109/CDC.1991.261604.

Verboven, P. (2002), "Frequency-domain system identification for modal analysis", Ph.D. Dissertation, Vrije University Brussel, Belgium.

Welch, P.D. (1967), "The use of fast Fourier transforms for the estimation of power spectra: a method based on time averaging over short modified periodograms", *IEEE Trans. Acoust. Speech*, **15**(2), 70-73. https://doi.org/10.1109/TAU.1967.1161901.

Wu, W.H., Wang, S.W, Chen, C.C. and Lai, G. (2016), "Mode identifiability of a cable-stayed bridge under different excitation conditions assessed with an improved algorithm based on stochastic subspace identification", *Smart Struct. Syst., Int. J*., **17**(3), 363-389. https://doi.org/10.12989/sss.2016.17.3.363.

Wu, W.H., Wang, S.W., Chen, C.C. and Lai, G. (2017), "Assessment of environmental and nondestructive earthquake effects on modal parameters of an office building based on long-term vibration measurements", *Smart Mater. Struct*., **26**(2017), 055034. https://doi.org/10.1088/1361-665X/aa6ae6.

Wu, W.H., Wang, S.W., Chen, C.C. and Lai, G. (2019), "Modal parameters identification for closely spaced modes of civil structures based on an upgraded stochastic subspace methodology", *Struct. Infrastruct. Eng*., **15**(3), 296-313. https://doi.org/10.1080/15732479.2018.1547770.

BS